KGi--186.

DETERMINATION OF THE THERMOSPHERIC NEUTRAL WIND FROM INCOHERENT SCATTER RADAR MEASUREMENTS

I. Häggström, J. Murdin and D. Rees

KGI REPORT NO. 186
November 1984

KIRUNA GEOPHYSICAL INSTITUTE
KIRUNA SWEDEN

DETERMINATION OF THE THERMOSPHERIC NEUTRAL WIND FROM INCOHERENT SCATTER RADAR MEASUREMENTS

by

I. Häggström and J. Murdin
Kiruna Geophysical Institute
P. O. Box 704
S-981 27 KIRUNA, Sweden

and

D. Rees
University College London, Gower Street
London WC1E 6BT England

KGI Report No. 186
November 1984

Printed in Sweden
Kiruna Geophysical Institute
Kiruna, 1984
ISSN 0347-6405

Determination of the Thermospheric Neutral Wind from Incoherent Scatter Radar Measurements

by

I. Häggström and J. Murdin
Kiruna Geophysical Institute
P.O. Box 704
S-981 27 KIRUNA, Sweden

and

D. Rees
University College London, Gower Street
London WC1E 6BT, England

Abstract

Measurements made by the EISCAT UHF incoherent scatter radar are used to derive thermospheric winds. The derived wind is compared to Fabry-Perot interferometer measurements of the neutral wind made simultaneously. The uncertainties in the radar derived wind are discussed.

Introduction

The meridional component of the thermospheric wind has been derived from incoherent scatter radar measurements by a number of authors, eg Evans (1971), Amayenc and Vasseur (1972).

Comparisions have also been made between the "radar" meridional wind and that measured by a Fabry-Perot interferometer, Burnside et al (1982). There have also been attempts to derive the zonal neutral wind from incoherent scatter radar measurements, Bates and Roberts (1977).

In this report we use EISCAT tristatic UHF measurements in order to derive both meridional and zonal components of the thermospheric neutral wind. The derived wind is compared to simultaneous optical measurements made by the UCL Fabry-Perot (D. Rees).

The emphasis here is on a description of the technique for deriving the "radar" neutral wind and a study of the limitations of the method. A full study of the ionospheric and neutral atmosphere interaction for the period of the measurements used here will be reported elsewhere, but we have included some model calculations that show the neutral wind fields and temperatures for different conditions.

Radar measurements

The data we have used were taken when EISCAT was operated in common mode zero November 25-26, 1982. In this experiment the Tromsö antenna is pointed parallel to the geomagnetic field at an altitude of 312 km and the remote antennae at Kiruna and Sodankylä are pointed to intersect the Tromsö beam at that point.

Two pulses are used in the transmission scheme. A 60 μs pulse for measurements of an altitude power profile, not used here, and a 360 μs pulse for autocorrelation function (ACF) measurements. From Tromsö 23 ACFs are measured, along the geomagnetic field line, with the first range gate at

a range of 130 km and with a range gate increment of 27 km. These ACF measurements have a range resolution of approximately 50 km although returns from a range interval of 108 km contribute to the ACF (eg Murdin 1981). The remote receiver stations also use the 360 μs pulse for ACF measurement. In this case, the altitude resolution is governed by the antenna beam width and is better than 10 km. The pulse repetition frequency was 125 Hz.

The data were post experiment integrated to an integration time of 5 minutes. The Tromsö ACFs were analysed to produce altitude profiles of electron density (n_e), electron and ion temperature (T_e, T_i), and the component of the ion drift velocity parallel to $\underline{B}$, $v_\parallel$ (positive up). An altitude model of ion compositon was used in the analysis which, however, in our main region of interest, around an altitude of 300 km, yields O^+ as the single ion species. The derived ion drift velocity component is not sensitive to the ion composition used in the analysis. The ACFs recorded at Kiruna and Sodankylä were analysed for an O^+ plasma using the modified pulse weighing function (Murdin 1983).

The three components of the ion drift velocity obtained at an altitude of 312 km were then combined to yield the vector drift velocity. Tne random errors in the plasma parameters derived from a single station ACF are a function of the signal to noise ratio and the integration time. Typically for an electron density of $3 \cdot 10^5$ cm $^{-3}$ at an altitude of 312 km the estimated standard deviations in n_e, T_e, T_i, and v_i are approximately

	$n_e(cm^{-3})$	$T_e(K)$	$T_i(K)$	$v_i(m/s)$
Tromsö	$0.01.10^5$	10	10	4
Kiruna	$0.02.10^5$	20	20	8
Sodankylä	$0.04.10^5$	40	40	15

The random error in the vector ion drift velocity is then a function of the individual station errors and the antenna

geometry. For the conditions above we obtain

	v_i(east)	v_i(north)	v_i(parallel)
$\sigma(ms^{-1})$	70	30	4

The data we have studied were taken over on almost 24 hour period 25-26 November 1982. The ion drift is displayed as a function of time in figure 1. Gaps in the data are due to data taking failure at one of the three receiver stations. The standard error is presented by a bar.

Neutral wind theory

Bates and Roberts (1977) described a method to calculate the neutral wind at F-region heights from incoherent scatter measurements of n_e, T_e, T_i, and $\underline{v}_i$. We follow their presentation but include the electron heating term in the ion energy equation and take account of the presence of an bi-Maxwellian ion velocity distribution and the velocity dependence of O^+-O collision frequency.

The ion energy equation and the electron and ion momentum equations are (Banks and Kockarts, 1973)

$$\frac{3}{2} n_i k \frac{\partial T_i}{\partial t} + \frac{3}{2} n_i k \underline{v}_i \cdot \nabla T_i + n_i k T_i \nabla \cdot \underline{v}_i + \nabla \cdot \underline{\Phi}_i =$$

$$= \sum_s \frac{2 m_i n_i \nu_{is}}{m_i + m_s} \left(\frac{3k}{2} (T_s - T_i) \Psi_{is} + \frac{m_s}{2} (\underline{v}_i - \underline{v}_s)^2 \Phi_{is} \right)$$

$$\frac{d\underline{v}_e}{dt} + \frac{1}{\rho_e} \nabla p_e - \underline{g} - \frac{q_e}{m_e} (\underline{E} + \underline{v}_e \times \underline{B}) = - \sum_s \nu_{es} (\underline{v}_e - \underline{v}_s) \Phi_{es}$$

$$\frac{d\underline{v}_i}{dt} + \frac{1}{\rho_i} \nabla p_i - \underline{g} - \frac{q_i}{m_i} (\underline{E} + \underline{v}_i \times \underline{B}) = - \sum_s \nu_{is} (\underline{v}_i - \underline{v}_s) \Phi_{is}$$

where we have used common notations. The index s stands for all species (electrons, ions, neutrals), $\underline{\Phi}$ is the heat flux vector. Ψ_{is}, Φ_{is}, and Φ_{es} are high speed correction terms, which accounts for changes in both relative speed and cross section, and the collision frequencies are in the laboratory frame of reference.

Parallel component

If we assume one type of ion, single charged and charge neutrality, and consider $m_e << m_i$, the ion and electron momentum equations parallel to the geomagnetic field yield (Häggström et al, 1983)

$$u_\parallel = v_\parallel - w_d$$

where $u_\parallel$, $v_\parallel$ are the components of the neutral wind and ion drift velocity parallel to the geomagnetic field $\underline{B}$ (positive up)

and w_d is the ambipolar diffusion velocity given by

$$w_d = \frac{1}{\sum_n \nu_{in}\Phi_{in}} \left(\frac{k}{n_e m_i} \frac{\partial}{\partial l} (n_e (T_e + T_i)) + g \sin I \right)$$

where l is a length along $\underline{B}$ and I the dip angle.

Meridional component

If u_N is the component of the neutral wind in the meridional plane perpendicular to $\underline{B}$

$$u_N = u_z \sec I - u_\parallel \tan I$$

where u_z is the vertical neutral wind component. Thus if

$$u_z = 0$$

$$u_N = u_\parallel \tan I$$

We can also note that if the magnetic field has a declination $\neq 0$, then the horizontal northward component of the

neutral wind is given by

$$u_{Ng} = - u_{\parallel} \sec I$$

Zonal component

The ion energy equation yields after neglecting transport, conduction, and time dependent terms

$$T_i - T_n = \frac{m_{eff}}{3k} (\underline{v}-\underline{u})^2 + \rho_e$$

$$\text{where } m_{eff} = \frac{\sum_n \frac{m_n \nu_{in} \Phi_{in}}{m_i+m_n}}{\sum_n \frac{\nu_{in} \Psi_{in}}{m_i+m_n}}$$

$$\text{and } \rho_e = \frac{\nu_{ie}(T_e-T_i)}{m_i \sum_n \frac{\nu_{in} \Phi_{in}}{m_i+m_n}}$$

The first term on the right stands for the Joule or frictional heating and the other, for electron heating of the ion gas. In the E-region the ion gas temperature is almost equal to the neutral gas temperature due to the frequent collisions between ions and neutrals. At F-region heigts the collision frequencies are low and electron heating raises the ion gas temperature above the neutral temperature. When there exists ion-neutral relative drift, Joule heating raises the ion gas temperature even more and it is possible to calculate the relative drift speed.

$$(\underline{u} - \underline{v})^2 = \frac{3k}{m_{eff}} (T_i - T_n) - \frac{3k}{m_{eff}} \rho_e \qquad (1)$$

Also

$$(\underline{u}-\underline{v})^2 = (v_E - v_E)^2 + (u_N - v_N)^2 + (u_\parallel - v_\parallel)^2$$

where u_E, v_E are the components of the neutral wind and ion drift velocity in zonal plane perpendicular to $\underline{B}$

and we obtain

$$u_E = v_E \pm \sqrt{(\underline{u} - \underline{v})^2 - (u_N - V_N)^2 - (u_\parallel - v_\parallel)^2}$$

with two solutions. We expect the ion drag to be the dominant force, and therefore, we choose the solution of the smallest magnitude.

For magnetic field declination ≈0 the geographic and magnetic eastward components of u are equal.

Bi-Maxwellian ion velocity distribution

Under condition of strong plasma convection and Joule heating it is not expected that the ion velocity distribution will remain Maxwellian (St. Maurice and Hanson, 1982). As a zeroth order approximation these authors consider the ion velocity distribution to be bi-Maxwellian with a higher perpendicular temperature ($T_\perp$) than that parallel ($T_\parallel$) to the geomagnetic field. If the radar scattering vector makes an angle θ with the geomagnetic field, then the one dimensional ion velocity distribution along the scattering direction is Maxwellian with temperature T, which is measured by the radar, given by

$$T = T_\parallel \cos^2\theta + T_\perp \sin^2\theta$$

St. Maurice and Hanson give

$$T_\parallel = T_i - \tau(\underline{v} - \underline{u})_\perp^2$$

$$T_\perp = T_i + \frac{\tau}{2}(\underline{v} - \underline{u})_\perp^2$$

where τ is a coefficient depending on the ion-neutral interaction.

Since

$$T_i = \frac{2T_\perp + T_\parallel}{3}$$

where T_i is the effective ion temperature,

we obtain

$$T_i = T + \tau(\underline{v}-\underline{u})_\perp^2 \left(1-\frac{3\sin^2\theta}{2}\right)$$

Method

We consider O^+ ion and $O/N_2/O_2/H_e$ neutral atmosphere. The neutral densities are taken from the MSIS-model (Hedin et al., 1979) and the rate coefficients for the ion-neutral collision frequencies are taken from Carlson and Harper (1977) (O^+-O) and Banks and Kockarts (1973)(O^+-N_2, O^+-O_2, O^+-H_e).

In the ambipolar diffusion velocity the pressure gradient is determined by measured values of $n_e(T_e+T_i)$ at five altitudes, which are fitted to a polynomial of the second order and derivated. At 312 km the ambipolar diffusion velocity varies between 5 and 40 m/s for this day and is thus of the same order as the parallel ion drift velocity. Figure 2 is an example of the altitude profiles of $v_\parallel$, $u_\parallel$, and w_d in a time sequence.

The rate coefficient given by Banks and Kockarts (1973) together with the measured electron density, yields the ion-electron collision frequency. The derived electron heating of the ion gas is at the most 30 K.

We use the Kiruna measured ion temperature T since this has excellent altitude resolution and better signal to noise ratio than Sodankylä. In this case $\theta=18^o$. τ is given for O^+-O and O^+-N_2 interactions (St Maurice and Hanson, 1982).

$$\tau = \frac{3.5 \cdot 10^{-4} \nu_{O+O} + 1.96 \cdot 10^{-4} \nu_{O+N_2}}{\nu_{O+O} + 1.11 \nu_{O+O} + 1.36 \nu_{O+N_2}}$$

For an ion-neutral relative drift $|\underline{v}-\underline{u}|$ of 1000 m/s the effective ion temperature is about 200 K above the Kiruna measured ion temperature.

The effects of Ψ_{in} and Φ_{in} are discussed in Häggström et al., 1983, and for $(T_i - T_n)$=1000 K $|\underline{v}-\underline{u}|$ is 200 m/s greater for hard sphere interactions, which we apply here, than for Maxwell molecules.

Since T_i and also Ψ_{in} and Φ_{in} are functions of $(\underline{v}-\underline{u})^2$, eq 1 takes an implicit character but it quickly comes to convergence after a few iterations. Finally we have taken the neutral temperature T_n as given by the MSIS-model.

Fabry-Perot interferometer

The instrumentation operated at KGI has been described in detail previously (Rees et al., 1981, 1983a, 1983b). Throughout the period of observations overlapping with the EISCAT measurements, the FPI was in its standard operating mode and tuned to the 630 nm O emission line. In this mode, the FPI makes a sequence of six observations of the horizontal wind in the directions N, NW, W, S, E, NE (at a zenith distance of 60 degrees) interspaced with a direct zenith view and a wavelength calibration frame. The total period of this sequence was throughout this observing period 16 minutes, with a two minute integration time in each direction. The 8-position sequence provides a monitor of the thermospheric wind and temperature in a region about 800 km diameter about Kiruna, assuming an emission altitude of 240 km, and the vertical wind component and temperature overhead at Kiruna.

At all times, but particularly during periods of strong geomagnetic activity, the thermospheric winds within the 800 km diameter region observed by the FPI may have large

horizontal gradients, and also show periods of rapid change of both meridional and zonal components. At the time of the observations reported here the FPI observations of horizontal wind components are made in regions of the order of 400 km distant from the region where ion drifts are directly sampled by EISCAT. Despite the strong time and spatial-dependent features of the FPI wind observations, thermospheric winds in the region sampled by EISCAT should be closely related to the averaged flows determined by the FPI.

Results

With the method described the neutral wind at 312 km has been derived from the radar data. In Figure 3 the geographic north component of the radar wind and the FPI measurements at north, where the vertical wind u_z is also assumed to be zero, are compared. The agreement is good. The vertical ion drift, v_z, is also plotted and the most serious discrepancies in the comparison appear to occur where v_z is most different from zero. Since the declination is almost zero (0.3^o), we have

$$u_{Nr} = u_z \tan I - u_{\parallel} \sec I$$

$$u_{No} = u_l \sec e - u_z \tan e$$

where r and o stand for radar and optical derived wind respectively. u_l is the line of sight velocity and e is the elevation of the Fabry-Perot. If we compare u_{Nr} and u_{No}, we obtain

$$u_{Nr} - u_{No} = u_z(\tan I + \tan e) - u_{\parallel} \sec I - u_l \sec e$$

The first term on the right is then an error term if u_z is assumed to be zero. So if $u_z>0$, then $u_{nr}<u_{no}$ if u_z is assumed to be zero and vice versa.

If vertical neutral motion is correlated to the strong vertical ion drifts observed, the neglect of the vertical component of the neutral wind would appear to explain the most serious discrepancies between the radar and optical estimates of u_N. In fig 3 we tend to observe that when $u_{Nr} < u_{No}$, we have strong upward ion drift, $v_z > 0$, and vice versa.

The FPI measurements vertically above Kiruna have indicated that the vertical neutral wind may reach magnitudes of the order of 50 ms^{-1}. Such a vertical neutral wind would lead to an error in the radar derived value of u_N of the order of 200 ms^{-1} and in the optical value of the order of 30 ms^{-1}.

The zonal radar wind and the FPI measurements at east are compared in Figure 4. Here the agreement is not very good but they exhibit similar trends. The major breakdown occurs after 0230 UT when the radar data lead to strong (≈250 m/s) westward winds at a time when the FPI shows a zonal wind of 50 m/s or less. This 'error' is coincident with the sudden rise of ion and neutral temperatures (Figure 4), the neutral temperature rise, of course, not being part of the model temperature (MSIS) used in the solution of the equations. We have preliminary optical measurements of T_n whose absolute values are in doubt but which, after 0230 UT, show significant increase. An increase in that 0230 could explain our bad agreement there.

Before 0230 UT the radar and the FPI follow the same trends with the radar wind being nearly twice as big as the FPI wind. The reason for this is partly due to the height difference and partly due to the radar field line being significantly north of the optical measurement (to the east of Kiruna), and we expect the neutral wind velocity on the average to be higher with greater altitude and latitude.

The sensitivity of the derived winds of the model density and temperature is shown in Figures 5 and 6. The effect of

altering the density of O, which is the most important neutral species at an altitude of 300 km, ±30% is relatively small for both the meridional and zonal components, ±25 m/s. On the other hand, when varying the neutral temperature by ±100 K, it has no effect on the meridional component, but the zonal component has very high sensitivity to this, ±100 m/s to ±300 m/s, the smaller the difference between ion and neutral temperatures the higher sensitivity.

Model calculations

The lack of a full three-dimensional and time dependent description of the background atmosphere leads to an irresolvable uncertainty of the order of 100-200 K for the neutral temperature anywhere in the vicinity of auroral regions.

We have used the UCL 3-D T-D global model (Rees et al., 1984) to show three examples of the neutral wind fields and temperatures at an altitude of 320 km and 18 degrees east longitude.

Model JC2 (Fig. 7)

This model corresponds to a simulation of moderate geomagnetic activity and with a positive sense of the IMF BY component. The B2 polar electric field of Heppner and Maynard (1983) is used to drive the northern hemisphere in this simulations.

Here we have strong westward winds sweeping to lower latitudes in the afternoon and southward winds during the magnetic midnight and the early AM hours reverting to weak westward before dawn.

In the polar cap, winds appear never to flow poleward, but change from westward (and possibly equatorward) early in the UT day, to eastward and equatorward late in the UT day. Very strong equatorward wind around midnight.

Model JB2 (Fig. 8)

This model corresponds to a similar level of geomagnetic activity as that generated in the JC2 model. However, in this simulation, the northern hemisphere is driven by the A2 polar convective electric field of Heppner and Maynard (1983), which, therefore, depicts conditions when the IMF BY component is negative.

We have westward winds in the afternoon, changing after 18 UT into strong eastward and southward winds in the auroral oval. In the polar cap, winds are poleward and westward early in the UT day and change to eastward later in the UT day.

Model JQ (Fig. 9)

This model corresponds to a simulation of enhanced ion-neutral momentum coupling. That is, the F-region electron densities are enhanced to simulate an increased level of energetic plasma precipitation, compared with those of the JC2 simulation. The B2 electric field is used again to simulate conditions with the IMF BY component positive.

The winds throughout the polar cap, but particularly on the dawn side, are considerably enhanced. In the auroral oval, the increased plasma densities increase sunward winds in both the morning and afternoon parts. In the auroral oval, the highest wind velocities are seen in the pre-midnight period. Winds should be strongly westward between 14 and 20 UT, and equatorward and eastward during the early morning hours, but comparatively weaker than during the afternoon period.

Comparison of temperature structures

Each of the three simulations produces a significant temperature enhancement in the high latitude regions, associated with the energy directly deposited by auroral electrons and also contributed by the combination of friction

and Joule heating. The simulations corresponding to IMV BY positive display their major enhancements in regions corresponding to the dawn side of the polar cap, where frictional heating appears to be very strong (i.e. the JC2 and JQ simulations). The JQ simulation, with the highest electron densities, shows the most spectacular temperature rise, which might be seen as a major post-midnight temperature bulge at a location such as Kiruna - the heating is poleward of Kiruna, but the heated air is carried there by the thermospheric horizonal wind circulation. When the IMF BY component is negative, the geomagnetic heating of the early morning region is greatly reduced, despite the larger ion flow velocities in the dawn auroral oval. In this case, the major heating region is around local noon, and on the dusk side of the polar cap, again where the anti-sunward ion flow velocities are largest.

Discussion and conclusions

With the tristatic capability of the EISCAT UHF radar it is possible to measure the ion drift velocity with excellent spatial and temporal resolution. The monostatic Fabry-Perot interferometer determines the line of sight neutral wind and thus cannot measure the vector neutral wind with good spatial resolution.

We have used the tristatic incoherent scatter radar measurements, with the same temporal and spatial resolution as the ion drift measurements, in order to derive estimates of the vector neutral wind. The comparisons made betweent the "radar" neutral wind and the "optical" neutral wind indicate that the method of determining the "radar" wind is promising, but also highlight the limitations of the method. Lack of knowledge of the vertical component of the neutral wind (we have assumed it is zero) and the neutral gas temperature (we have assumed MSIS model values) produce large uncertainties in the "radar" neutral wind.

However, a Fabry-Perot interferometer observing vertically upwards through the radar scattering volume would produce estimates of the vertical component of the neutral wind and neutral temperature, however, with some uncertainty in the altitude of the measurements. We propose to carry out such an experiment in the future, lowering the radar scattering volume to about 240 km altitude. We hope thus to be able to determine both the ion drift velocity and the neutral wind with the same excellent spatial and temporal resclution. Such measurements can be important in monitoring the local interaction betweeen ion and neutral motion.

References

Amayenc. P., and G. Vasseur, Neutral winds deduced from incoherent scatter observations and their theoretical interpretation, J. Atmos. Terr. Phys., 34, 351-364, 1972.

Banks, P.M., and A. Kockarts, Aeronomy, Academic Press, New York, 1973.

Bates, H.F., and T.D. Roberts, A technique for using incoherent scatter to estimate F-region zonal winds during Joule Heating, J. Atmos. Terr. Phys., 39, 1293-1306, 1977.

Burnside, R.G., R.A. Behnke, and J.C.G. Walker, Meridional neutral winds in the thermosphere at Arecibo: Simultaneous incoherent scatter and airglow observations, J. Geophys. Res., 88, 3181-3189, 1983.

Carlson, H.C., and R.M. Harper, An experimental estimate of the O^+-O resonant charge transfer cross section, collision frequency and energy transfer rate, J. Geophys. Res., 82, 1144-1148, 1977.

Evans, J.V., Observations of F-region vertical velocities at Millstone Hill 1. Evidence for drifts due to expansion, contraction and winds, Radio Sci., 6, 609-626, 1971.

Hedin, A.E., J.E. Salah, J.V. Evans, C.A. Reber, G.P. Newton, N.W. Spencer, D.C. Kayser, D. Alcayde, P. Bauer, L. Cogger and J.P. McClure, A global thermospheric model based on mass spectrometer and incoherent scatter data. MSIS 1. N_2 density and temperature, J. Geophys. Res., 82, 2139-2147, 1977.

Hedin, A.E., C.A. Reber, G.P. Newton, N.W. Spencer, H.C. Briton, and M.G. Mayer, A global thermospheric model based on mass spectrometer and incoherent scatter data. MSIS 2. Composition, J. Geophys. Res., 82, 2148-2156, 1977.

Häggström, I., A. Pellinen, and J. Murdin, Collision frequencies in the ionosphere, KGI Report 180.

Murdin, J., Measurement of autocorrelation functions in a bi-static incoherent scatter radar, J. Atmos. Terr. Phys., 45, 67-72, 1983.

Rees, D., P.A. Rounce, P. Charleton, T.J. Fuller-Rowell, I. McWhirter and K. Smith, J. Geophys., 50, 202, 1981.

Rees, D., C.R. Philbrick, M. Carlson, T.J. Fuller-Rowell and P. Charleton, "Adv. in Space Res." (Pergamon), 2, No 10, 129, 1983a.

Rees, D., P. Charleton, M. Carlson and P. Rounce, High latitude thermospheric circulation during the Energy Budget Campaign, Submitted to J. Atmos. Terr. Phys., 1983b.

Rees, D., M.F. Smith, and Gordon, Generation of vertical thermospheric winds and gravity waves at auroral latitudes. Paper II. Theory and numerical modelling of vertical winds, Submitted to Planet. Space Sci., 1984.

St.-Maurice, J.-P., and W.B. Hanson, Ion frictional heating at high latitudes and its possible use for in situ determination of neutral thermospheric winds and temperatures, J. Geophys. Res., 87, 7580-7602, 1982.

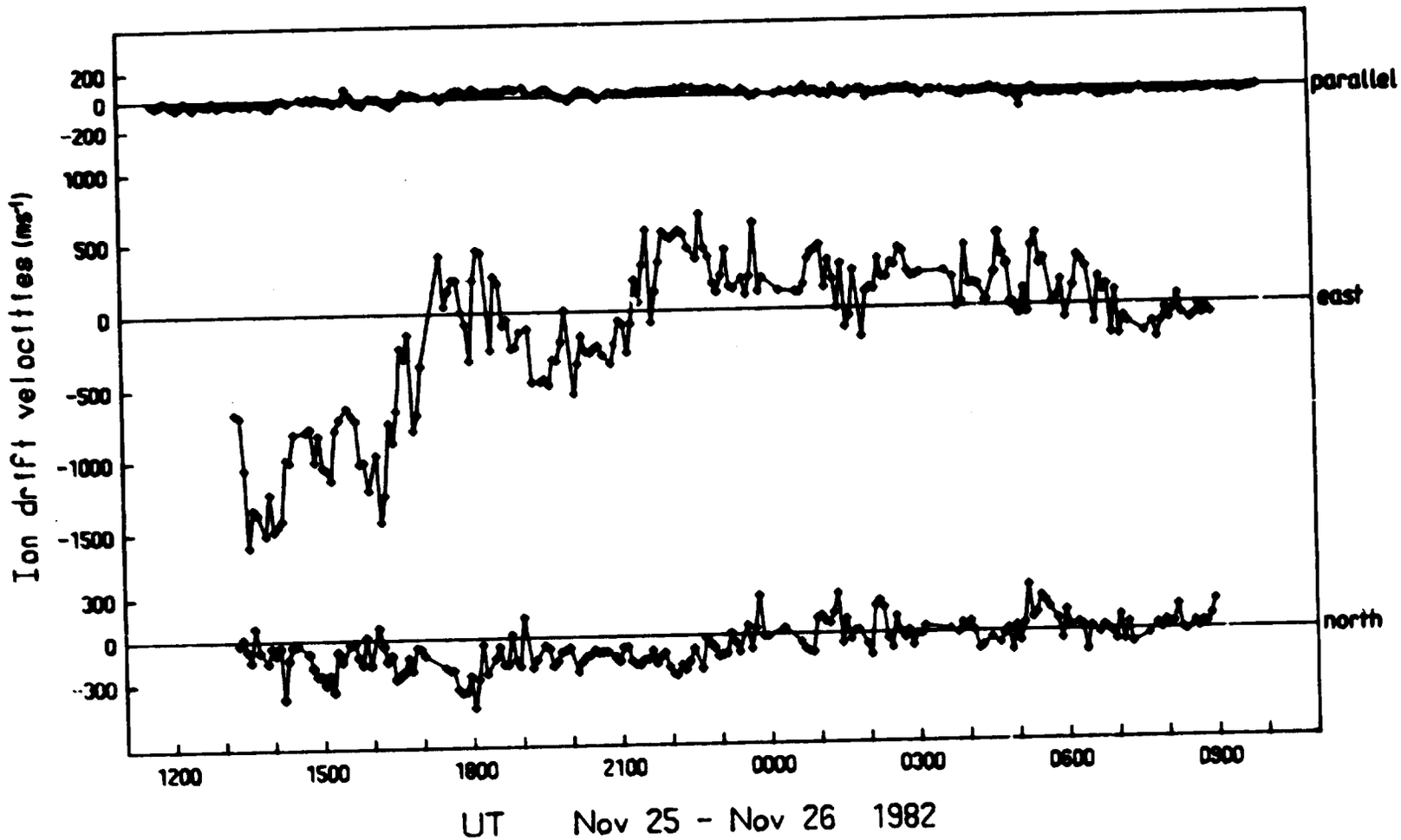

Figure 1 Ion drift velocity in geomagnetic frame. From top parallel the field lines (positive up), East and North. The scale marked on the left is in ms^{-1}.

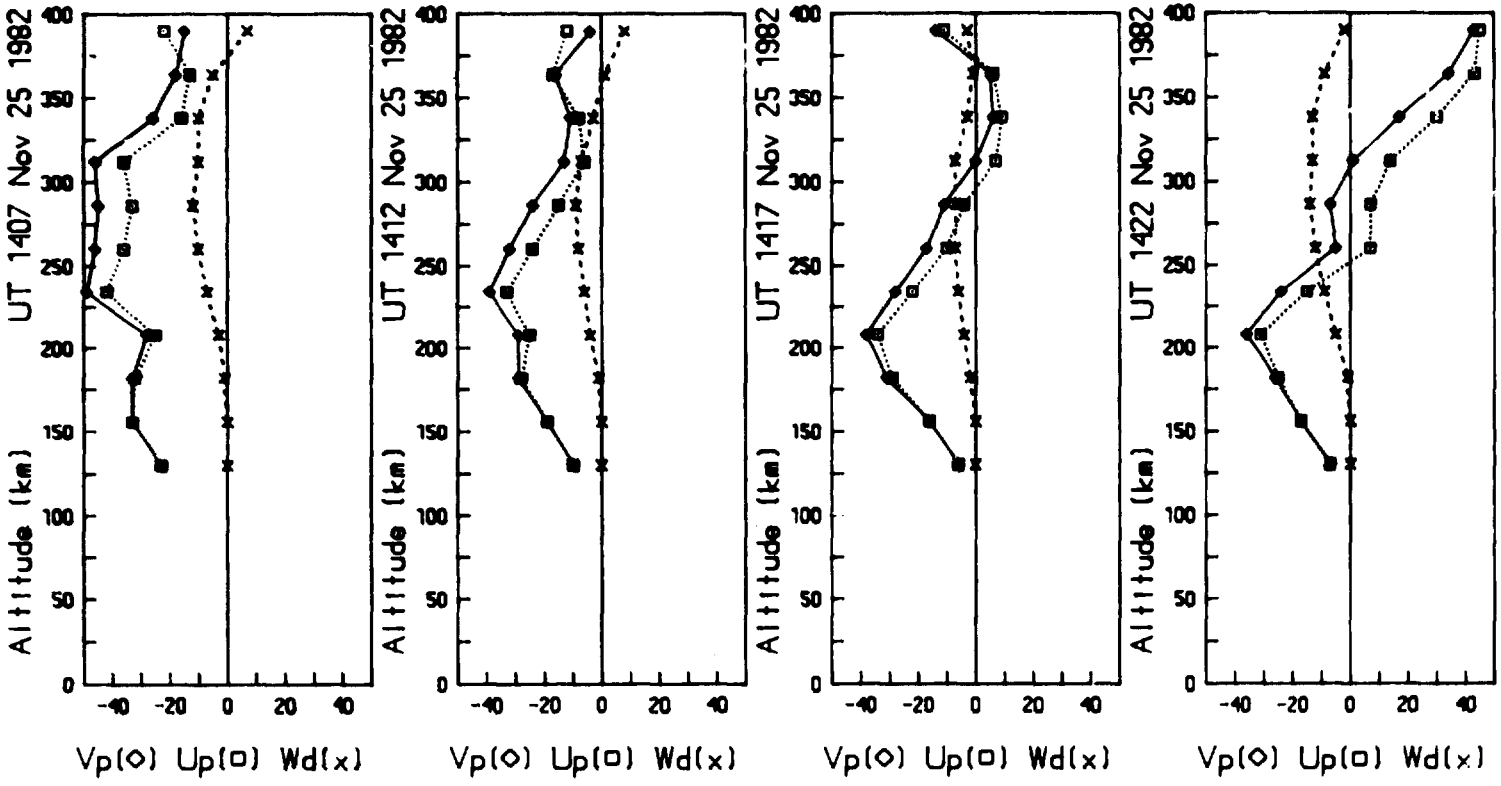

Figure 2 Altitude profiles of v_p (diamonds), w_d (crosses), and u_p (squares) in a time sequence. The scale marked on the left is in km and at the bottom ms^{-1}.

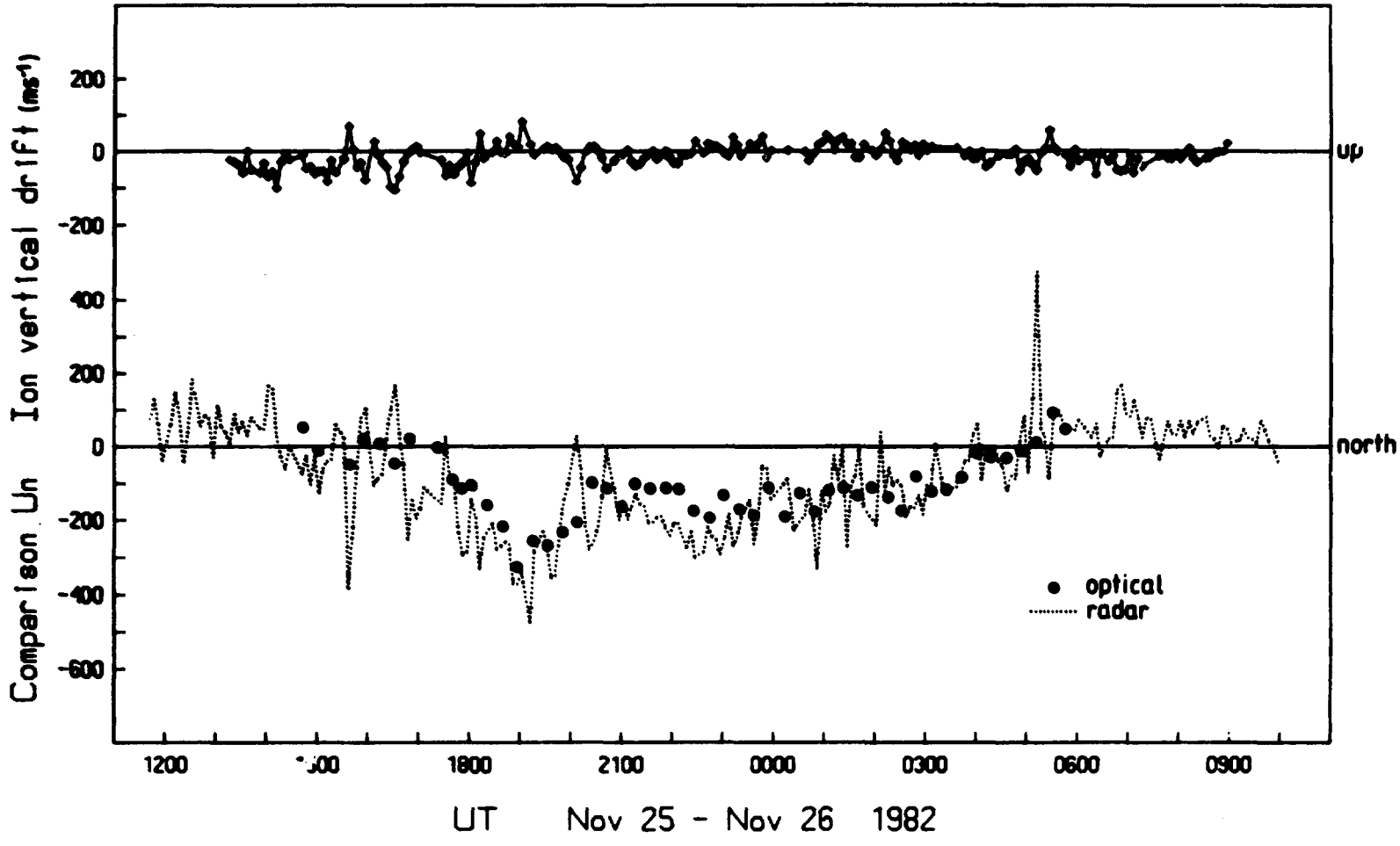

Figure 3 Comparison of the meridional neutral wind derived from the EISCAT data (dotted line) and the FPI wind in the north (points). The top panel shows the vertical ion drift. The scale marked on the left is in ms^{-1}.

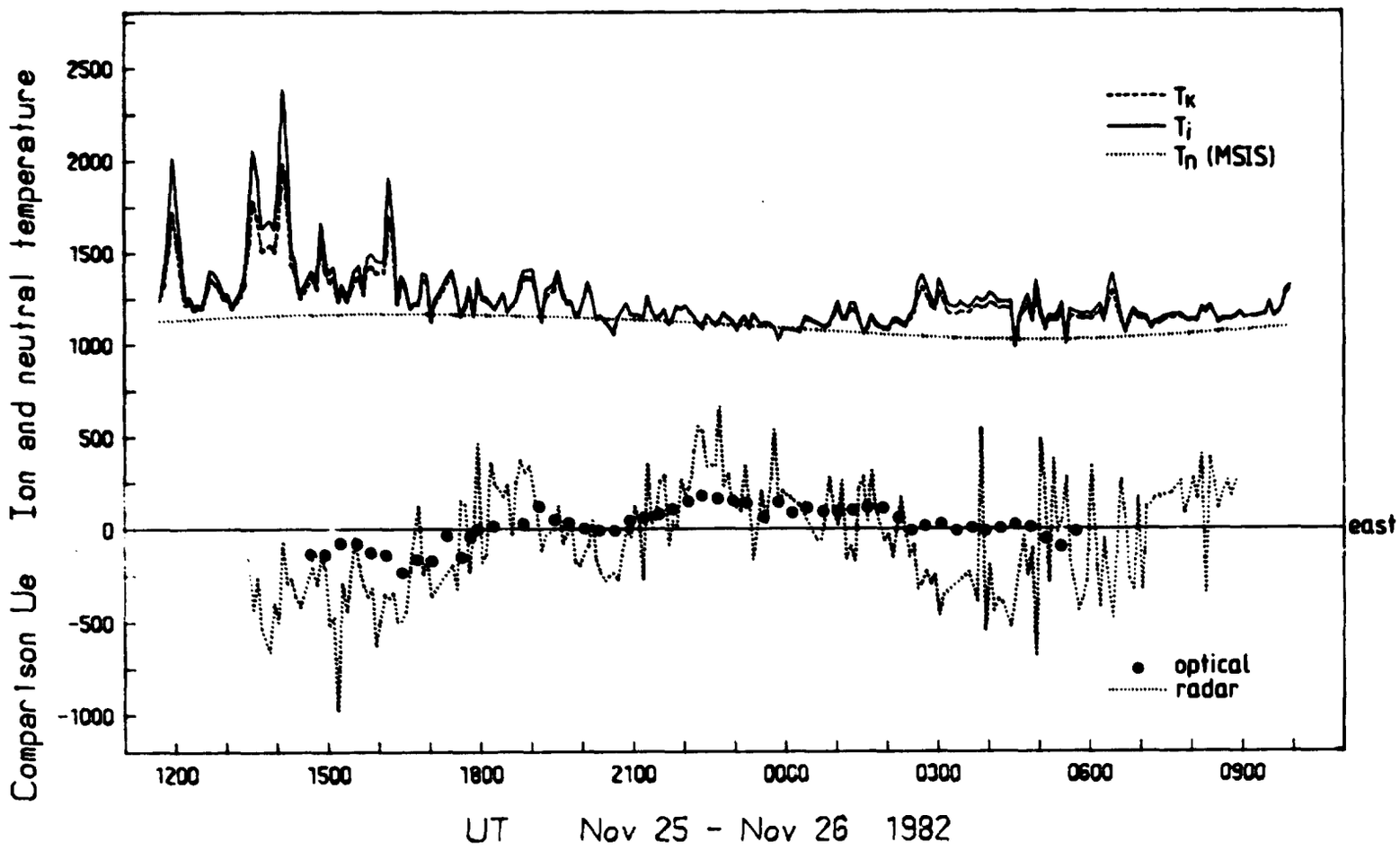

Figure 4 Comparison of the zonal neutral wind derived from the EISCAT data (dotted line) and the FPI wind in the east (points). At the top, the derived ion temperature (solid line), the measured ion temperature at Kiruna (dashed line) and the MSIS neutral temperature (dotted line).

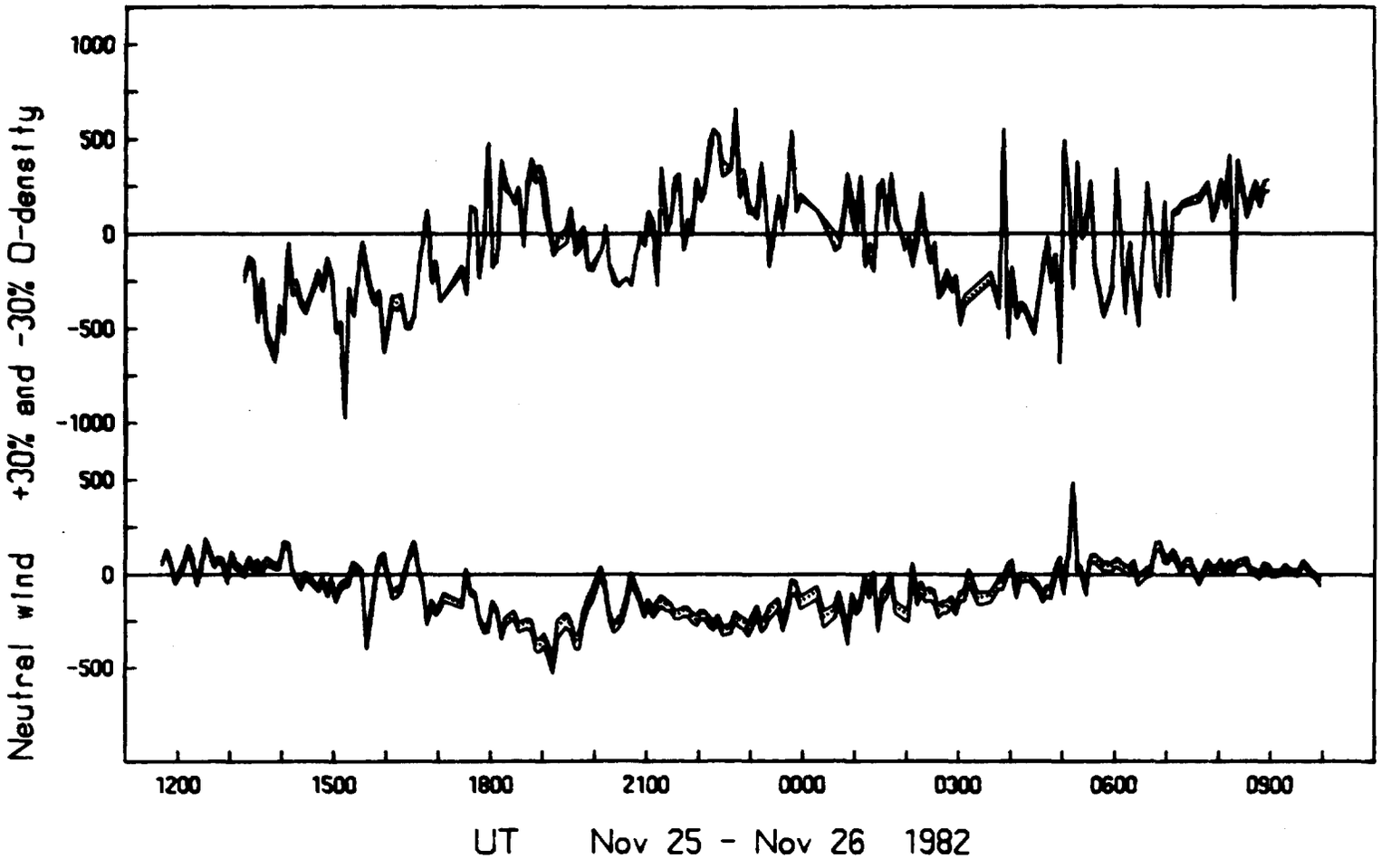

Figure 5 Sensitivity study of O density for the zonal and meridional component. The dotted lines are the unchanged components and the solid lines are the components when the MSIS O-density is changed by +30% and -30%.

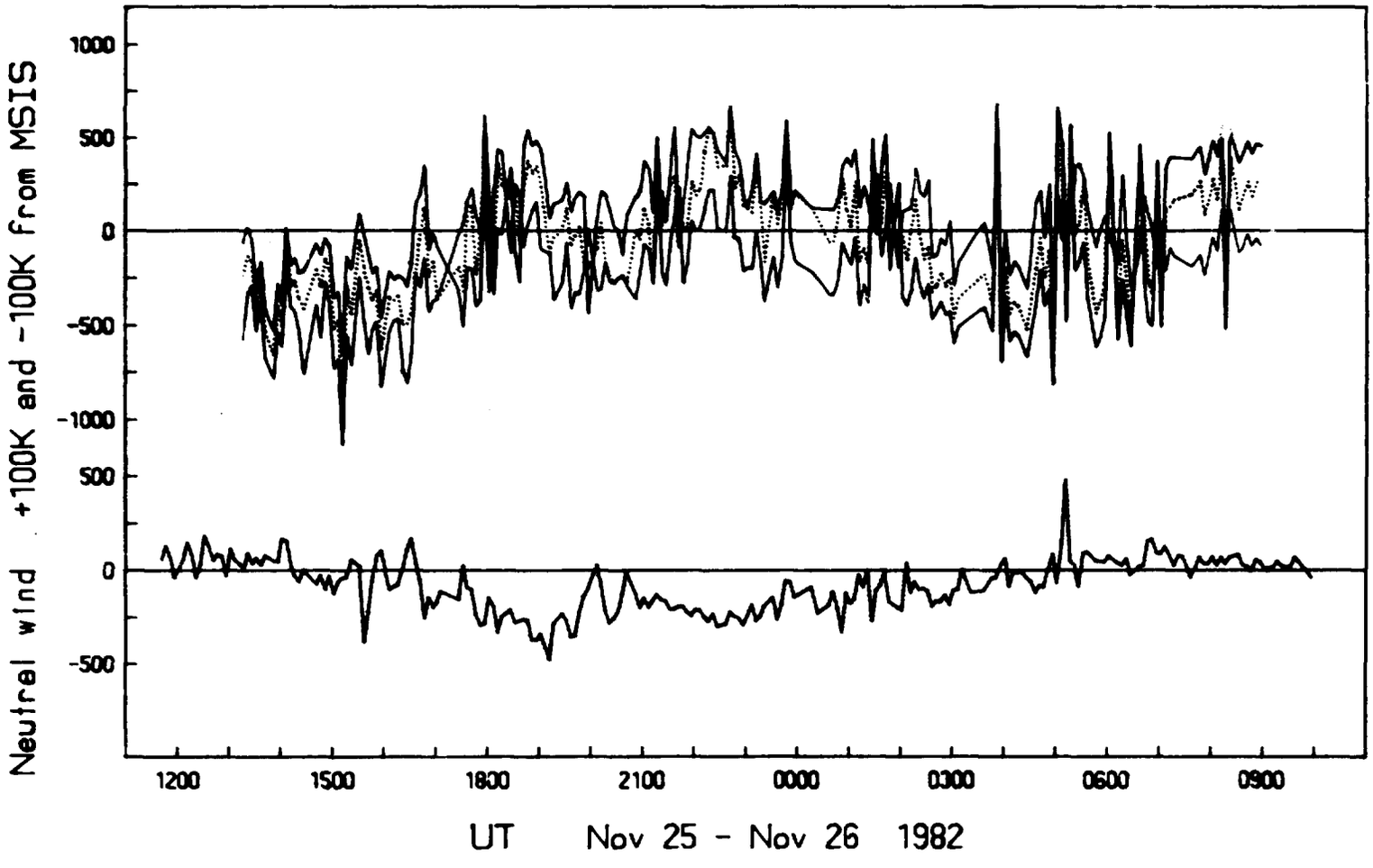

Figure 6 Sensitivity study of neutral temperature for the zonal and meridional component. The dotted lines are the unchanged components and the solid lines are the components when the MSIS neutral temperature is changed by +100 K and -100 K.

Figure 7 Model JC2 of neutral wind flow and temperature with B2 polar convective field by Heppner and Maynard (1983) with IMF BY component positive.

Figure 8 Model JB2 of neutral wind flow and temperature with A2 polar convective field by Heppner and Maynard (1983) with IMF BY component negative.

Figure 9 Model JQ of neutral wind flow and temperature as, JC2 but for enhanced ion-neutral momentum coupling.

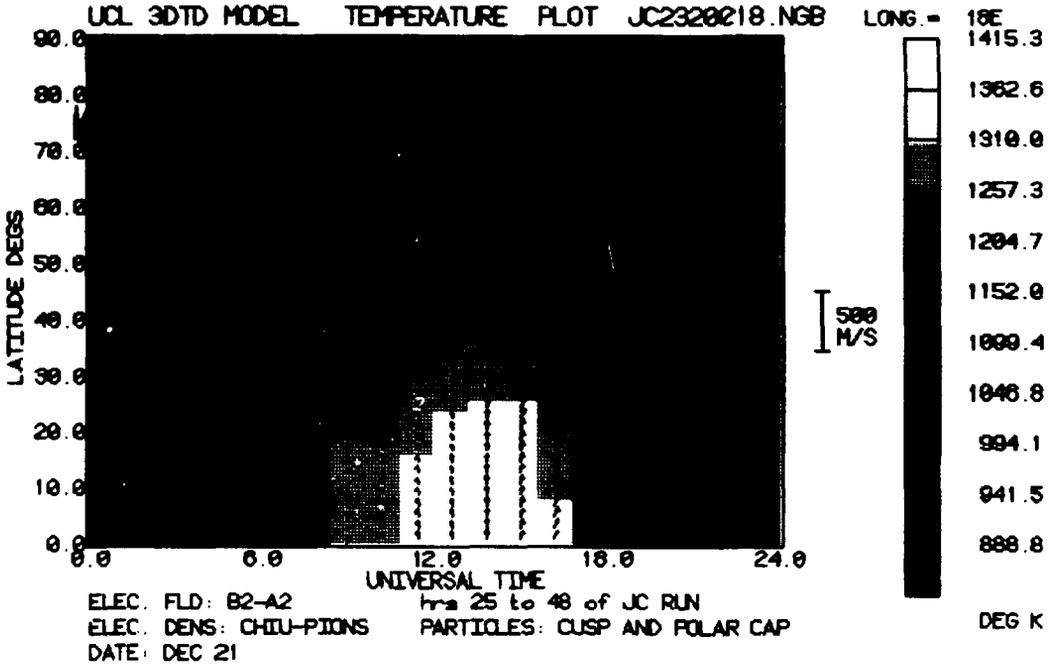
UCL 3DTD MODEL TEMPERATURE PLOT JC2320018.NGB
LONG.= 18E
LATITUDE DEGS
90.0
80.0
70.0
60.0
50.0
40.0
30.0
20.0
10.0
0.0
0.0
6.0
12.0
18.0
24.0
UNIVERSAL TIME
500 M/S
1415.3
1362.6
1310.0
1257.3
1204.7
1152.0
1099.4
1046.8
994.1
941.5
888.8
DEG K
ELEC. FLD: B2-A2
Hrs 25 to 48 of JC RUN
ELEC. DENS: CHIU-PIONS
PARTICLES: CUSP AND POLAR CAP
DATE: DEC 21

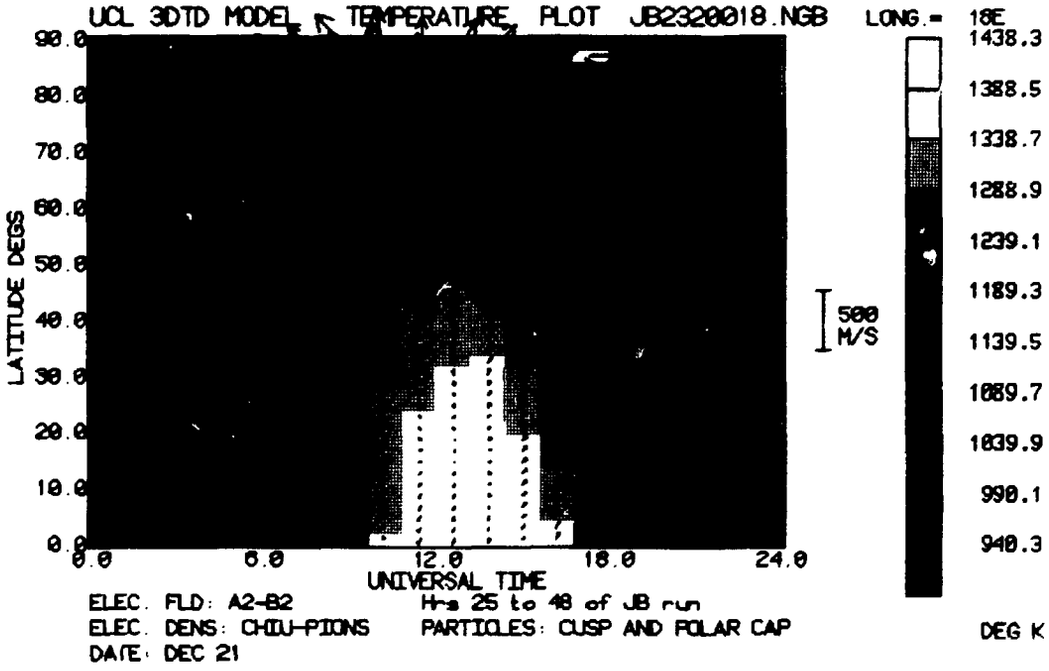
UCL 3DTD MODEL TEMPERATURE PLOT JB2320018.NGB
LONG.= 18E
LATITUDE DEGS
90.0
80.0
70.0
60.0
50.0
40.0
30.0
20.0
10.0
0.0
0.0
6.0
12.0
18.0
24.0
UNIVERSAL TIME
500 M/S
1438.3
1388.5
1338.7
1288.9
1239.1
1189.3
1139.5
1089.7
1039.9
990.1
940.3
DEG K
ELEC. FLD: A2-B2
Hrs 25 to 48 of JB run
ELEC. DENS: CHIU-PIONS
PARTICLES: CUSP AND POLAR CAP
DATE: DEC 21

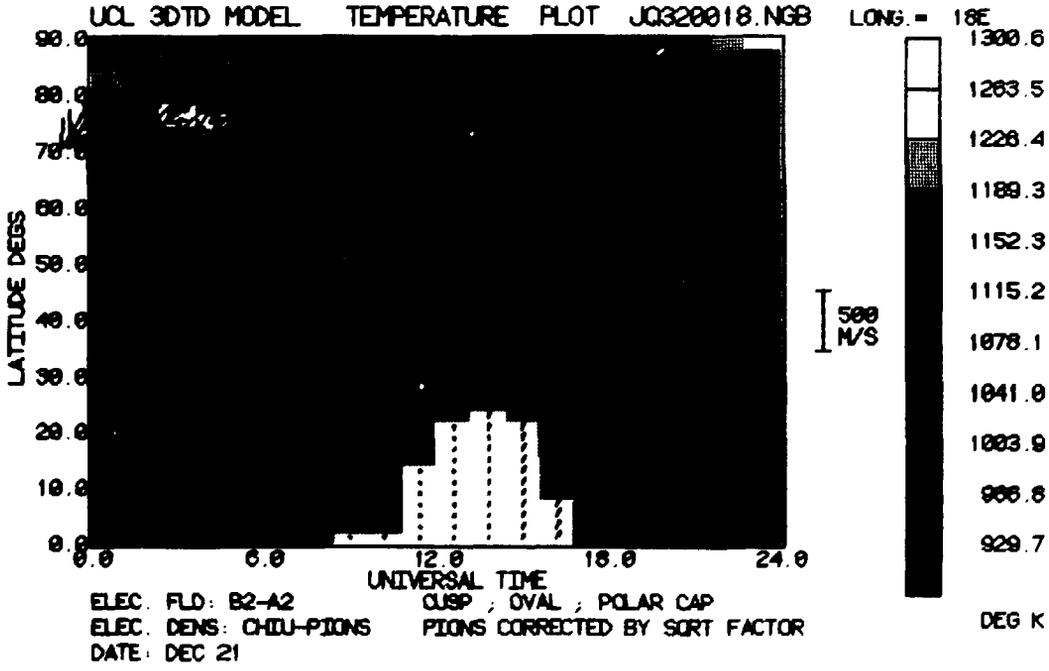
UCL 3DTD MODEL TEMPERATURE PLOT JC3200018.NGB
LONG.= 18E
LATITUDE DEGS
90.0
80.0
70.0
60.0
50.0
40.0
30.0
20.0
10.0
0.0
0.0
6.0
12.0
18.0
24.0
UNIVERSAL TIME
500 M/S
1300.6
1263.5
1226.4
1189.3
1152.3
1115.2
1078.1
1041.0
1003.9
966.8
929.7
DEG K
ELEC. FLD: B2-A2
CUSP ; OVAL ; POLAR CAP
ELEC. DENS: CHIU-PIONS
PIONS CORRECTED BY SQRT FACTOR
DATE: DEC 21